Ocean Science
Discussions

Open Access

Tidal forcing, energetics, and mixing near the Yermak Plateau

I. Fer[1,3], M. Müller[2], and A. K. Peterson[1,3]

[1]Geophysical Institute, University of Bergen, Bergen, Norway
[2]Norwegian Meteorological Institute, Oslo, Norway
[3]Bjerknes Centre for Climate Research, Bergen, Norway

Correspondence to: I. Fer (ilker.fer@gfi.uib.no)

OSD

11, 2245–2287, 2014

Tidal mixing near the Yermak Plateau

I. Fer et al.

Title Page

Abstract	Introduction
Conclusions	References
Tables	Figures

|◄ | ►|
◄ | ►
Back | Close

Full Screen / Esc

Printer-friendly Version

Interactive Discussion

Abstract

The Yermak Plateau, located northwest of Svalbard in Fram Strait, is the final passage for the inflow of warm Atlantic Water into the Arctic Ocean. The region is characterized by the largest barotropic tidal velocities in the Arctic Ocean. Internal waves generated in response to the tidal flow over this topographic feature locally contribute to mixing and remove heat from the Atlantic Water. Here, we investigate the tidal forcing, barotropic-baroclinic energy conversion rates, and dissipation rates in the region using observations of oceanic currents, hydrography and microstructure collected on the southern flanks of the plateau in summer 2007, together with results from a global high resolution ocean circulation and tide model simulation. The energetics (depth-integrated conversion rates, baroclinic energy fluxes and dissipation rates) show large spatial variability over the plateau and are dominated by the K_1 and M_2 constituents. The volume-integrated conversion rate over the region enclosing the topographic feature is approximately 1 GW and accounts for about 50 % of the M_2 and approximately all of the K_1 conversion in a larger domain covering the entire Fram Strait extended to the North Pole. Despite the substantial energy conversion into internal tides, a negligible fraction propagates out of the YP region, implying large local dissipation rates. An approximate local conversion – dissipation balance is found over shallows and also in the deep part of the sloping flanks. The baroclinic energy radiated away from the upper slope is dissipated over the deeper isobaths. From observations below the surface mixed layer, we infer upper and lower bounds on the total dissipation rate of about 0.5 and 1 GW, where about 0.4 GW can be attributed to the contribution of hot spots. The domain-integrated dissipation from the model is close to the upper bound of the observed dissipation, and implies that almost entire dissipation in the region can be attributed to the dissipation of baroclinic tidal energy.

Title Page

Abstract | Introduction

Conclusions | References

Tables | Figures

Back | Close

Full Screen / Esc

Printer-friendly Version

Interactive Discussion

1 Introduction

The Yermak Plateau (YP, Fig. 1), located northwest of Svalbard is the main topographic obstacle for the warm Atlantic inflow to the Arctic Ocean. The Marginal Ice Zone (MIZ), the transition region between open waters and dense ice cover, is typically located
5 over the plateau, indicating substantial oceanic heat loss to melting of sea ice in the region. The YP is identified as a region of enhanced tidal variability for both diurnal and semidiurnal tides (Hunkins, 1986; Padman et al., 1992; D'Asaro and Morison, 1992; Plueddemann, 1992). Strong tidal currents over the sloping flanks of the plateau lead to increased internal wave activity and diapycnal mixing of water properties (Padman
10 and Dillon, 1991; Wijesekera et al., 1993; Fer et al., 2010). The mixing in this region is of particular interest because it can contribute to cooling of the West Spitsbergen Current carrying warm and saline Atlantic Water through Fram Strait. The heat removed from the Atlantic layer can influence the inflowing water properties to the Arctic, and the regional ice cover north of Svalbard.
15 Breaking of internal waves is a major source of turbulence-driven diapycnal mixing in the ocean. One generation mechanism for internal waves is the baroclinic response to barotropic tidal flow of a stratified water column over favourable topography, such as a continental slope, isolated ridge, or rough topography (Garrett and Kunze, 2007). Near generation sites, some of the energy locally dissipates through breaking of high-
20 mode, small scale waves (e.g., Klymak et al., 2008), whereas the remainder propagates as low-mode internal waves. At the latitudes of the YP, however, both the diurnal and the principal semidiurnal tidal frequency M_2 linear internal waves are evanescent and cannot propagate freely (the inertial frequency defined by the latitude-dependent Coriolis parameter is larger than the wave frequency). As we show in the following, the
25 YP is a site of substantial barotropic to baroclinic energy conversion. It is expected that the baroclinic energy extracted from the surface tide dissipates locally, and contributes to turbulent mixing.

Estimates from global numerical models on the conversion rates of barotropic to baroclinic tidal energy in the Arctic region amount to about 5 GW (Simmons et al., 2004; Müller, 2013). There are several detailed numerical model studies on the energetics of internal tides for specific, energetic regions like the Hawaiian Ridge and Monterey Canyon (e.g., Merrifield and Holloway, 2002; Kang and Fringer, 2012); however, regional studies on high-latitude internal tides are still missing. In general, the generation of near-inertial and sub-inertial internal tides has not obtained a lot of attention, although there are strong signs that they have the potential to impact decadal climate variations (Tanaka et al., 2012; Müller, 2013).

Earlier investigations in the YP region typically used observations of hydrographic properties and velocity of the water column sampled from ice camps or autonomous buoys along their transpolar drift (see Padman et al., 1992; Fer et al., 2010, for an overview). Measurements of ocean currents from a drifting buoy showed that energy increased threefold from its level in the Nansen Basin as the buoy passed over the YP (Plueddemann, 1992), dominated by peaks at the diurnal and near-inertial (semidiurnal) period motions. Energetic bursts of near-inertial internal wave packets were inferred to propagate upwards, presumably generated by interaction of tide with the bottom. Similarly, D'Asaro and Morison (1992) identified upward propagating near-inertial waves and enhanced eddy diffusivity over the central plateau. Average ocean-to-ice heat flux of $22 \, \mathrm{W \, m^{-2}}$ was inferred from an automated buoy as it drifted over the northern YP (McPhee et al., 2003). In the pycnocline above the Atlantic layer, Padman and Dillon (1991) observed an upward heat flux of $25 \, \mathrm{W \, m^{-2}}$, which decreased to $6 \, \mathrm{W \, m^{-2}}$ below the surface mixed layer. These mixing rates and heat fluxes are comparable to those observed over the shelves north of Svalbard and in proximity to West Spitsbergen Current branches (Fer and Sundfjord, 2007; Sirevaag and Fer, 2009). Our study differs from the earlier work in that we report observations from stations, each occupied typically for one day duration, and a 8 day long time series from a bottom-anchored mooring. The data set is presented earlier in Fer et al. (2010, F2010 henceforth), who reported strong variability in internal wave activity and vertical mixing at the YP. The

Printer-friendly Version

Interactive Discussion

rate of conversion of surface tide energy to baroclinic energy, the spatial distribution of the baroclinic energy fluxes and energy dissipation rates, however, are unknown. Here, we hypothesize that spatially varying tides and their baroclinic response over topography are responsible for the observed variability and mixing.

5   In this paper we discuss tidal forcing and the role of tides in mixing near the Yermak Plateau. The observational data set is supplemented with results from a global high resolution ocean circulation and tide model simulation (STORMTIDE, Müller et al., 2012), to obtain barotropic-baroclinic energy conversion rates and baroclinic energy fluxes in the region. Our results have relevance for the Arctic Ocean where the maximum tidal

10   velocities of 5–10 cm s^{-1} (Kowalik and Proshutinsky, 1993) are sufficient to generate observable internal waves over suitable topography such as mid-basin ridges and the continental shelf break.

2   Methods

2.1   Observational data

15   The site and measurement details are described fully in F2010; only a brief summary is given here. Observations were made in summer 2007 from the Research Vessel *Håkon Mosby* in the southern YP. Sampling was limited by the ice-edge in the MIZ, and included five stations and an 8-day long time series from a mooring (Fig. 1 and Table 1). Each station was occupied for approximately one day. Full-depth CTD (conductivity,

20   temperature, depth) profiles were collected using a Sea-Bird Scientific SBE911*plus* system. At each station ocean microstructure profiles were taken approximately every 30–60 min (222 casts in total) in the upper 520 m using a loosely-tethered free-fall profiler equipped with shear probes (MSS, manufactured by ISW Wassermesstechnik, Germany). Velocity in the water column was measured by a vessel-mounted

25   Teledyne RD Instruments (RDI) Narrowband 150 kHz acoustic Doppler current profiler (VM-ADCP) in the upper 360 m. Additionally, at Station 1, 6 velocity profiles at

Tidal mixing near the Yermak Plateau

I. Fer et al.

Title Page

Abstract	Introduction
Conclusions	References
Tables	Figures

|◄ | ►|

◄ | ►

Back | Close

Full Screen / Esc

Printer-friendly Version

Interactive Discussion

approximately 4 h interval were collected to the bottom, using eXpendable Current Profilers (XCP).

The mooring was deployed at a water depth of 889 m, co-located with Station 5. The mooring line was instrumented with 19 SBE37 Microcats recording conductivity, temperature and (16 of them) pressure, distributed between 99–873 m; a Teledyne RDI 75 kHz Longranger ADCP at approximately 2 m above the bottom looking upward and sampling in 8 m bins; and an Aanderaa (Xylem Inc.) Seaguard current meter at 23 m depth. Sampling interval was one minute for all moored instruments. With the exception of the Longranger that stopped after 15 h because of a leakage, all moored instruments sampled throughout the deployment.

Post-processing of the CTD and current measurements follows common procedures and is briefly summarized in F2010. Post-processing of the microstructure data follows Fer (2006), see also F2010. Profiles of dissipation rate of turbulent kinetic energy (TKE) per unit mass, ε, are obtained from the shear probes to a noise level of 3–5×10^{-10} W kg^{-1}. The reduced data set collected from the vessel and used in the analysis includes current profiles from the VM-ADCP (hourly temporal and 4 m vertical average) and XCPs (2 m vertical average), temperature, salinity and potential density anomaly, σ_θ, profiles from the ship's CTD and from the MSS (1 m vertical average), and dissipation rate ε from the MSS (1 m vertical average). The data set from the mooring includes hourly averaged and vertically gridded horizontal velocity and σ_θ profiles at 8 and 20 m vertical resolution, respectively.

2.2 Numerical modelling

The numerical model is a global high-resolution ocean circulation and tide model coupled to a thermodynamic sea-ice component (STORMTIDE, Müller et al., 2012). The STORMTIDE model implicitly resolves internal waves and the meso-scale ocean circulation. It is formulated on a global tripolar grid with an average horizontal resolution of about 10 km, which becomes as small as 5 km in high latitudes. The model physics and numerics are based on the Max-Planck Institute Ocean Model (Jungclaus et al.,

2006). The astronomical tidal forcing is described by ephemerides and represents the complete lunisolar tidal forcing of second degree. The model uses no internal wave drag, i.e. no additional energy sink for barotropic tides in the deep ocean. The conversion of barotropic to baroclinic tidal energy (Sect. 3.1) amounts to 1.14 TW in the deep ocean, and is in the range of previous estimates from models, theory, and observations (Egbert and Ray, 2000; Simmons et al., 2004; Nycander, 2005).

A ten year STORMTIDE simulation is used in the present study, and a detailed description on the set-up of the model simulation including atmospheric forcing, restoring schemes, and physical parametrization can be found in Müller et al. (2014). The hourly output of 32 days of sea level and velocities, starting 1 January, have been used for a harmonic analysis with respect to several tidal constituents (Foreman et al., 2009). Global model products of tidal velocities, energetics, and sea level are available for download at the World Data Centre for Climate (see Müller et al., 2014, for details). The barotropic and low-mode internal tides have been evaluated in Müller et al. (2012). It has been shown that the surface internal tide signature, evaluated by sea surface satellite products, is reasonably well captured. The barotropic-tide-induced sea level variability is captured to 93% and a recent barotropic tide model intercomparison shows that STORMTIDE ranks similar to other modern hydrodynamic tide models (Stammer et al., 2014).

3 Methods of analysis

In order to characterize the tidal forcing and energetics at the YP region and at the observation stations, the STORMTIDE and the cruise data, respectively, are used. The methods involved are summarized below.

3.1 Tidal energy conversion and energy fluxes in STORMTIDE

The simulated tidal energy flux and conversion of barotropic to baroclinic tidal energy is computed by using the derivations presented in Kang and Fringer (2012). The vertically-integrated, baroclinic tidal energy flux with zonal and meridional components, $\mathbf{F} = (F_u, F_v)$, is calculated from

$$\mathbf{F} = \langle \overline{\tilde{p}\tilde{\boldsymbol{u}}} \rangle_t \tag{1}$$

where $\tilde{p}$ is the perturbation pressure associated with tidal motions and $\tilde{\boldsymbol{u}}$ is the baroclinic tidal current vector. $\langle \cdot \rangle_t$ and the overbar denote averages in time and integral in the vertical, respectively. The vertically-integrated, barotropic to baroclinic tidal energy conversion rates are derived from

$$C = \langle \overline{g\tilde{\rho}W} \rangle, \tag{2}$$

where $\tilde{\rho}$ is the density perturbation associated with the tidal motion and g the gravitational acceleration. The barotropic vertical velocity $W(z)$ at depth z is defined as

$$W(z) = -\nabla_H \cdot [(z+d)\boldsymbol{u}_{BT}], \tag{3}$$

where d is the total water depth, ∇_H is the horizontal differential operator, and $\boldsymbol{u}_{BT}$ the horizontal barotropic tidal current vector. We further derive baroclinic radiation defined as the horizontal divergence of the baroclinic energy flux, $\nabla_H \cdot \mathbf{F}$, and define the depth-integrated dissipation, $C - \nabla_H \cdot \mathbf{F}$, as the difference between tidal energy conversion and radiation (e.g., Kang and Fringer, 2012).

3.2 Energy and energy flux from observations

The calculation of the baroclinic energetics follows the common methods, see e.g., Kunze et al. (2002) and Nash et al. (2005). For a sinusoidal wave, the calculation

requires perturbation profiles of velocity and pressure isolated at the corresponding frequency band, sampled over the whole water column, for an integer number of wave periods. We apply harmonic analysis to determine the amplitude and phase of the semidiurnal wave, generate full-period time series and project them onto flat-bottom

5   vertical modal shapes to obtain full-depth profiles at each station. Subsequent sections detail the methods involved in each step. $\langle \cdot \rangle_z$ and $\langle \cdot \rangle_\phi$ indicate averaging over depth and (semidiurnal) wave period, respectively. At all stations, density profiles are available for approximately two semidiurnal cycles (day-long time series). Comparably long time series are obtained from VM-ADCP at stations 1, 2 and 4 (Table 1). Stations 3 and 5

10   however, have too short VM-ADCP sampling duration to resolve the semidiurnal wave and are excluded from the analysis. Near full-depth, between 23–864 m, 15.1 h-long current profiles recorded by the moored instruments allow for energy flux calculations at the mooring location near Station 5.

3.2.1 Baroclinic perturbation calculations

15   Baroclinic velocity is calculated at each time by removing the depth-averaged profile, $u_{BC}(z,t) = u(z,t) - \langle u(z,t) \rangle_z$. The depth average is an approximation to the barotropic velocity, and is valid because the shear in the surface and bottom boundary layers is not resolved by the moored instruments and the VM-ADCP. Baroclinic perturbation fields of velocity, u', vertical displacement, ξ, and reduced pressure, p', (pressure anomaly

20   divided by the mean density ρ_0) are calculated similar to the methods described in Kunze et al. (2002) and Nash et al. (2005). Baroclinic perturbation velocity is $u'(z,t) = u_{BC}(z,t) - \langle u(z,t) \rangle_t$. Vertical isopycnal displacement profiles, $\xi(z,t)$, are constructed by interpolating to depth from displacements of isopycnals from their station time-mean depth, $\xi(\sigma_\theta, t) = z(\sigma_\theta, t) - \langle z(\sigma_\theta, t) \rangle_t$. For the mooring data, displacements are calculated

25   relative to 24 h moving average density profiles.

Barotropic flow over a sloping bottom induces (barotropic) vertical displacement which increases linearly with depth (Baines, 1982). Following Kunze et al. (2002), we remove this barotropic contribution, estimated by fitting a line with zero intercept to

each vertical displacement profile. Pressure anomalies are inferred from ξ assuming a hydrostatic balance (valid for the semidiurnal frequency), integrating with depth and removing the full-depth average in order to ensure that perturbation pressure is baroclinic (has zero depth average). The latter condition does not affect the depth-integrated baroclinic energy flux **F** (see Sect. 3.3). Reduced pressure anomaly in units of $J\,kg^{-1}$ is

$$p'(z,t) = \overline{\langle N^2(z,t)\rangle_t\, \xi(z,t)} - \langle\, \overline{\langle N^2(z,t)\rangle_t\, \xi(z,t)}\, \rangle_z, \tag{4}$$

where $N = -[(g/\rho_0)(\partial\sigma_\theta/\partial z)]^{-1/2}$ is the buoyancy frequency, ρ_0 is the reference density, and the overbar denotes integration with respect to depth as before.

3.2.2 Semidiurnal fits

In order to infer the baroclinic semidiurnal energy flux, we isolate the semidiurnal band in the perturbation time series. The semidiurnal frequency $\omega_{M2} = 1.405 \times 10^{-4}\,s^{-1}$ ~ 0.0804 cph (cycles per hour) is sub-inertial at 80° N where the inertial frequency is $f = 1.44 \times 10^{-4}\,s^{-1}$ ~ 0.0825 cph ~ $1.025\omega_{M2}$, and the two frequencies cannot be distinguished because of short record length. Therefore semidiurnal must be understood as the near-inertial band when discussing observations. The semidiurnal fluctuation $\tilde{x}_{M2}$ of a perturbation variable x' is estimated using harmonic analysis:

$$\tilde{x}_{M2}(z,t) = \langle x'\rangle_t + x_{M2}(z)\cos\left(\omega_{M2}t - \phi^x_{M2}(z)\right)$$

by minimizing the residual $R(z)$ in a least-square sense to determine the coefficients in

$$x'(z,t) = A(z)\cos(\omega_{M2}t) + B(z)\sin(\omega_{M2}t) + R(z),$$

where the amplitude profile is $x_{M2}(z) = (A(z)^2 + B(z)^2)^{1/2}$ and the phase profile is $\phi^x_{M2}(z) = \arctan(B(z)/A(z))$. The harmonic analysis is applied to $\boldsymbol{u}'$, ξ and p'. Semidiurnal fits for the horizontal velocity components explain 30–90 % of the total variance at the stations, whereas the semidiurnal vertical displacement accounts for relatively less (5–60 %) of the observed variance.

Tidal mixing near the Yermak Plateau

I. Fer et al.

3.2.3 Vertical modes

Constructed full period baroclinic semidiurnal time series are used to derive full depth profiles of $\tilde{u}$, $\tilde{\xi}$ and $\tilde{p}$. At each time, the corresponding vertical profile is projected onto orthogonal vertical modes with vertical structure G_j of each mode j governed by (Phillips, 1977)

$$\frac{d^2 G_j(z)}{dz^2} + \left[\frac{N^2(z)}{c_j^2} \right] G_j(z) = 0, \tag{5}$$

where c_j is the eigenspeed. Vertical velocity and vertical displacement structure of each mode scale with G_j, while the horizontal velocity is proportional to dG_j/dz. Eq. (5) is solved numerically for each station, using the station mean $N^2(z)$ and the boundary conditions $G_j(-H) = G_j(0) = 0$, where H is the total depth. Modal amplitudes are then obtained by least-squares fitting (stable solutions are obtained for the first three baroclinic modes). The full-depth profiles can then be constructed as the sum over modes as, for example, $\tilde{u}(z,t) = \sum \mathbf{U}_j(t) dG_j(z)/dz$, where $\mathbf{U}_j$ is the amplitude of the horizontal velocity for mode j. When averaged over each station's duration, the first three modes account for 50–80 % of the semidiurnal velocity and 25–75 % of the semidiurnal isopycnal displacement.

3.2.4 Wentzel–Kramers–Brillouin scaling

Although the stations are closely spaced, the stratification differs significantly as a result of lateral gradients in proximity to the ice edge (see F2010). In order to account for the varying stratification, we apply Wentzel–Kramers–Brillouin (WKB) scaling (Leaman and Sanford, 1975) using the survey mean stratification of $N_0 = 2.4 \times 10^{-4}\,\mathrm{s}^{-1} \equiv 1.38$ cph as the reference buoyancy frequency. The stretched depth for a given station mean $N(z)$ profile is $z_{\mathrm{wkb}} = \int_z^0 N(z)/N_0 dz$. Horizontal velocity and pressure scale as

$(N_0/N(z))^{1/2}$, and vertical velocity and displacement scale as $(N(z)/N_0))^{1/2}$. Table 1 lists the stretched water depth and the percentage of the stretched water column covered by the instruments. Although the sampling was limited to the upper 520 m (MSS) and 360 m (VM-ADCP), 64–99 % (MSS) and 49–73 % (VM-ADCP) of the stretched water column were covered. The portion of the mooring densely equipped with the Microcats covers 75 % of the stretched depth.

3.2.5   Energy and energy flux calculations

Full-depth and full-period baroclinic semidiurnal fields are constructed as the sum of the first three baroclinic modes. Baroclinic horizontal kinetic energy (HKE) and available potential energy (APE) in units of $J\,m^{-3}$ are obtained from

$$\text{HKE}(z) = \frac{\rho_0}{2}\langle \tilde{u}(z,t)^2 + \tilde{v}(z,t)^2 \rangle_\phi$$
$$\text{APE}(z) = \frac{\rho_0}{2}\langle N(z)^2 \rangle_t \, \langle \tilde{\xi}(z,t)^2 \rangle_\phi. \tag{6}$$

The vertically-integrated horizontal baroclinic energy flux is obtained as

$$\mathbf{F} = \overline{\langle \tilde{\boldsymbol{u}}(z,t)\tilde{p}(z,t)\rangle_\phi}. \tag{7}$$

We focus only on the vertically-integrated baroclinic energy flux, because of the ambiguity in determining the constant of integration to estimate the flux profiles over topography (Gerkema and van Haren, 2007).

3.3   Errors and uncertainty

In our study, following the common practice, we fix the constant by the baroclinicity condition for pressure, which is not valid near topographic features. The depth-integrated fluxes are independent of this integration constant, and can be used with confidence

(Gerkema and van Haren, 2007). The calculations, however, suffer from the short sampling duration, and from the uncertainty propagated from modal fits to vertically gappy sampling. Errors and systematic bias for a variety of sampling schemes are discussed in Nash et al. (2006). Full depth profiles sampled by 6 profiles spanning 15 h lead to estimates of semidiurnal depth-integrated energy flux with 10 % error, unbiased estimates can be computed by 4 profiles over 12 h. This error is representative of our XCP sampling at Station 1 with 6 casts spanning 20 h. For the case of vertically gappy sampling, larger gaps can be tolerated near the bottom after WKB scaling (as in the case of our MSS and VM-ADCP sampling), but estimates are sensitive to the data near the surface. This, however, ignores the possible contamination of the semidiurnal band by the near-inertial frequency non-tidal waves at high latitudes. Our sampling scheme is imperfect, both vertically and temporally, but has a reasonably good coverage of the stretched water column with typically 20–26 (MSS and hourly-averaged VM-ADCP) profiles spanning two semidiurnal cycles. We expect unbiased estimates with error less than 50 % in our semidiurnal depth-integrated energy flux calculation.

The semidiurnal fits to the observations are obtained by harmonic anaylsis using ω_{M2} only (Sect. 3.2.2). When the harmonic analysis is repeated using two constituents ($\omega_{K1} = 7.292 \times 10^{-5}\,\text{s}^{-1}$ and ω_{M2}), the variance explained by M_2 is within 5 % of the values obtained using the M_2 constituent only. At Stations 1 and 2, where there are long enough VM-ADCP data to fit both constituents, K_1 accounts for 20–25 % of the horizontal velocity. Diurnal vertical displacement accounts for 20–40 % at Stations 1 to 4 and dominate (57 %) at Station 5. The diurnal component is clearly important at the YP, but it is significantly sub-inertial. Because of the short station durations, we do not report diurnal baroclinic fluxes from the observations, but discuss them using the STORMTIDE model results.

Since the STORMTIDE model is a global hydrodynamic model, the horizontal and vertical resolution can not compete with regional models resolving non-linear characteristics of internal wave propagation (e.g., Simmons et al., 2011). Thus the model results are limited in their interpretation for linear wave characteristics. The dissipation

of internal waves is driven by numerical parametrization of bottom friction and eddy viscosity and further by numerical dissipation. In previous STORMTIDE model studies it has been shown that the internal wave generation and propagation of internal tides are reasonably well represented when compared to satellite altimetry products. Around hot spot regions in the deep ocean, the magnitude of the surface signature of internal tides is reasonably well reproduced. Further, the magnitudes and the regional characteristics of barotropic to baroclinic tidal conversion rates have proved to be similar to those in other models, observational and theoretical studies, which gives us confidence to apply the STORMTIDE model products to the Yermak Plateau.

4 Variability at the observation stations

Observations in 2007 were made during neap and transition to spring tides (Fig. 2). The data show strong variability in velocity and vertical isopycnal displacement in both diurnal and semidiurnal bands. Tidal surface elevation inferred at the model grid point nearest to the mooring location shows a tidal range of up to ±0.5 m, and both its phase and magnitude agree with the record inferred from the moored pressure sensor nearest to the seabed (Fig. 2a), lending further confidence on the model output. The duration of the current record is short, and the depth-average current suggests other contribution in addition to tidal flow. The time-depth maps of the vertical isopycnal displacement recorded by the moored instruments show up to ±40 m alternating bands with mixed diurnal and semidiurnal periodicity. On the southern flanks of the plateau, tidal ellipses derived from STORMTIDE show comparably strong semidiurnal (M_2) and diurnal (K_1) currents (not shown). Frequency spectra of total velocity at the pycnocline presented in F2010 correspond to about three times larger HKE in the diurnal band compared to the semidiurnal band. In agreement with the velocity spectrum, the diurnal band is the most energetic in the vertical isopycnal displacement spectra throughout the water column at the mooring location (F2010).

An overview of the semidiurnal amplitudes obtained from the harmonic analysis of the horizontal current and isopycnal displacements at Stations 1, 2, and 4 is given in Fig. 3. Station 2 has baroclinic semidiurnal amplitudes comparable to the barotropic tide, whereas at the other stations the barotropic component is larger. Overall, the semidiurnal current amplitudes are weak, typically one order of magnitude smaller than those near the Hawaiian Ridge (Nash et al., 2006) and about half of those at the Mendocino Escarpment (Althaus et al., 2003). Nevertheless, the semidiurnal signal accounts for a significant percentage of the observed profiles (Sect. 3.2.2). At Station 1, baroclinic vertical displacement is typically less than the barotropic component. In the upper 150 m of Stations 2 and 4 and between 200 and 300 m at Station 4, baroclinic vertical displacement exceeds the barotropic contribution. The phase of the horizontal current increases approximately linearly with depth at Station 1, indicating upward energy propagation with a vertical wavelength of at least 500 m. This is supported by the vertical wavenumber spectra obtained for the bottommost 512 m of the full-depth shear profiles sampled by XCPs suggesting upward energy propagation (F2010). The phase of the vertical displacement, on the contrary, typically decreases with depth. This can be a consequence of the sub-inertial semidiurnal waves trapped along the topography. At Stations 2 and 4, phase profiles show 180° jumps suggesting a vertically standing behaviour.

Baroclinic energy and energy fluxes inferred from full-depth profiles for the first mode and the sum of the first three modes are summarized in Table 2. The ratio R of depth-averaged HKE to APE for the sum of first three modes varies between 3 and 16 at the stations occupied by the ship, but it increases to 120 at the mooring. The latter can be because of the different record duration used in the harmonic fits to velocity (15.1 h) and vertical displacement (8 days). The ratio HKE/APE is equivalent to the shear-strain ratio R_ω discussed in F2010. The range 3–16 is typical for oceanic values and is consistent with the values inferred in F2010. Estimates from the XCP data at Station 1 are significantly different than those from the MSS/VM-ADCP profiles, suggesting that

the lack of MSS/VM-ADCP sampling in the deepest $\sim 50\,\%$ of the stretched depth significantly affects the results.

The horizontal components of the depth-integrated baroclinic energy flux are listed in Table 2. Here, **F** is directed nearly along the isobaths when derived from the MSS/VM-ADCP profiles, but is directed westward, away from the plateau when derived from the XCP profiles (Table 2). This is expected if there is M_2 internal tide radiation away from the plateau in the deeper half of the water column that dominates the depth-integrated flux. At Stations 2 and 4, and at the mooring location, the vertical coverage is better and we do not expect biased results. An alternative method is to calculate the energy flux from amplitude and phase of the semidiurnal baroclinic velocity and pressure (Arneborg and Liljebladh, 2009). If the water column is well resolved, this method is relatively accurate, since it does not rely on normal modes analysis which is questionable over sloping topography. Using the harmonic analysis results obtained for Station 4 and the mooring data, which cover about 73–75 % of the stretched water column (Table 1), the depth-integrated baroclinic energy fluxes agree to within 20–52 % of the values listed in Table 2, consistent with our choice of 50 % error (Sect. 3.3).

A station-mean profile of dissipation rate ε measured by the microstructure profiler is obtained by averaging over all profiles collected at each station (Fig. 4). Station 4 has the largest dissipation rates. Depth-integrated dissipation rates are given in Table 3. Station 4 profile extends to the bottom; observations at other stations, however, are limited to 500 m depth. Because the turbulence near the surface layer can be dominated by other processes than internal wave-induced mixing, values integrated between 50 and 500 m depth are also listed. In order to have an estimate of the full-depth (below 50 m) integrated ε for all stations, we construct a lower bound (ε_{min}) and an upper bound (ε_{max}) profile down to the mean echo depth of each station. Profiles of ε_{max} are obtained by extending the 450–500 m average value to the bottom (Fig. 4). Observed profiles at Stations 1 and 5 reach the noise level of $5 \times 10^{-10}\,\mathrm{W\,kg^{-1}}$ below about 150 m, suggesting that actual values can be lower. The profiles of ε_{min} are therefore constructed by exponentially reducing the 450–500 m average value for Stations

Title Page

Abstract | Introduction

Conclusions | References

Tables | Figures

|◄ | ►|

◄ | ►

Back | Close

Full Screen / Esc

Printer-friendly Version

Interactive Discussion

2 and 3, and the value at 200 m for Stations 1 and 5, to an assumed low dissipa-
tion of 10^{-10} W kg^{-1} over a 200 m vertical scale, and extending this value to the bottom
(Fig. 4). Depth-integrated dissipation below the surface mixed layer is typically between
0.2 and 0.8×10^{-3} W m^{-2} on the southwest flanks, and increases by approximately
a factor of two at Station 4.

5   Energetics from the model

Barotropic tidal fluxes inferred from STORMTIDE are shown in Fig. 5. The semidiur-
nal tide has a typical poleward flux, whereas the diurnal tidal flux is diverging over the
plateau with near zero values on the eastern side of the plateau. These can be com-
pared to the K_1 and M_2 tidal fluxes around Svalbard shown in Chen et al. (2009): The
limited region shown in Fig. 5 is part of a pattern in which the M_2 energy propagates
clockwise around the Svalbard islands, whereas the K_1 tidal energy is mainly trapped
along the steep bottom topography. Both the K_1 and M_2 tidal fluxes are elevated along
the shelf break north of Spitsbergen and also along the outer flank of the plateau, par-
ticularly close to the CEAREX-O camp drift site. Near this site, the dispersion curves for
shelf waves suggest that both K_1 and O_1 waves can exist and propagate freely (Pad-
man et al., 1992). These regions of large barotropic fluxes are also associated with
high conversion rates and depth-integrated baroclinic fluxes (Fig. 6).

The baroclinic fluxes in the energetic parts of the YP are on the order of 200 W m^{-1} ($\equiv$
0.2 kW m^{-1}) for M_2 and 1 kW m^{-1} for K_1. For comparison, depth-integrated semidiurnal
energy fluxes over significant topographic features are 1–40 kW m^{-1} near the Hawaiian
Ridge (Rudnick et al., 2003), 3 kW m^{-1} near the Aleutian Ridge (Cummins et al., 2001),
2.4 kW m^{-1} at the Great Meteor Seamount (Gerkema and van Haren, 2007), and 5.5
kW m^{-1} for the Luzon Strait (Klymak et al., 2011). The shelf break in the east Japan Sea
is characterized by seasonal variations between 2 and 10 kW m^{-1} (Jeon et al., 2014).
Model-inferred depth-integrated M_2 baroclinic energy flux in the Monterey Submarine
Canyon region is typically 1–2 kW m^{-1} (Kang and Fringer, 2012); observations show

Title Page

Abstract | Introduction

Conclusions | References

Tables | Figures

◄ | ►

◄ | ►

Back | Close

Full Screen / Esc

Printer-friendly Version

Interactive Discussion

an increase to $5\,\mathrm{kW\,m^{-1}}$ at the canyon mouth (Kunze et al., 2002) and a decrease to $0.5\,\mathrm{kW\,m^{-1}}$ on the California continental margin south of Monteray Bay (Terker et al., 2014). Near our mooring location, the depth-integrated energy flux is one order of magnitude smaller than at many of these sites, and is reduced by another order of magnitude at the other stations.

Barotropic to baroclinic energy conversion rate, C, is shown for the semidiurnal and the diurnal tide in Fig. 6. The CEAREX-O site is characterized by moderate M_2 but substantially larger K_1 conversion rates, reaching $0.05\,\mathrm{W\,m^{-2}}$; the fluxes echo this pattern. The model results are thus consistent with the observations from the CEAREX-O camp where energetic internal waves and enhanced mixing were measured (Padman and Dillon, 1991). Negative conversion rate occurs when energy is transferred from baroclinic tide to the barotropic tide and indicates interaction between locally and remotely generated baroclinic tides (Kang and Fringer, 2012). Relatively large semidiurnal fluxes can be observed, directed toward shallower water, on the western part of the plateau around $82°\,\mathrm{N}$, and also along the shelf break north of Spitsbergen. The observational stations are characterized by weak conversion rates and depth-integrated baroclinic fluxes, **F**, except near Stations 1 and 5 on the western slope. From the model, **F** is calculated as the average over grid points within $10\,\mathrm{km}$ in the vicinity of each station. The results, together with one standard deviation, are listed in Table 4 for the major diurnal and semidiurnal constituents. The variability at neighbouring grid points is large. While the M_2 and K_1 constituents are the largest, S_2 and O_1 fluxes are comparable. The fluxes inferred from the observations (for M_2 only) compare fairly well with the model results (compare Tables 2 and 4), when averaged in the vicinity of the station location; however the comparison is poor when a single data point from the nearest grid to the station is used. Observed flux vectors are smaller than the size of the station markers in Fig. 6a, hence they are not shown. (A direct comparison on map is presented in Sect. 6.)

The conversion rates in the vicinity of the stations are dominated by the M_2 and K_1 constituents (3 to 10 times larger than S_2 and O_1), with values between 1 and

10×10^{-3} W m^{-2}, and with largest rates near Station 1. Dissipation rates at the station positions are weak, similar for M_2 and K_1, and vary between order 10^{-3} W m^{-2} (Station 2) and order 10^{-2} W m^{-2} (Station 1). Limited by the ice edge, the occupied observational stations are not representative of the energetics of the Yermak Plateau. In the following we shall rely on the model results to discuss the energetics in the region and its role for vertical mixing.

The baroclinic radiation and depth-integrated dissipation rates are obtained from the model (Sect. 3.1). A negative radiation is horizontal convergence of the depth-integrated flux and indicates that the location is a sink, whereas positive radiation indicates that the site is a source for baroclinic energy. In order to calculate volume-integrated conversion, radiation and dissipation rates, we define the YP region bounded between 5° W and 25° E zonally, 79° N and 83°30′ N meridionally, and by the 250 m isobath north of Svalbard. Surface area in this domain with water depth deeper than 250 m is approximately 2×10^{11} m^2, with a mean water depth of 2300 m. The volume-integrated conversion rate in the region is 322 MW for M_2 and 618 MW for K_1. The radiation is 8 and 1 MW, respectively. This indicates that despite substantial energy conversion into internal tides, only a minute fraction (if any) propagates out of the region, suggesting substantial local dissipation. The spatial distribution of depth-integrated dissipation rate for the M_2 and K_1 components is shown in Fig. 7.

The conversion is spatially variable, and is particularly concentrated near the 2000 m isobath in the northern flanks of the plateau (Fig. 6). Dissipation is typically elevated where the conversion rates are large and the spatial distribution is characterized by several regions (hot spots) where the dissipation is enhanced (Fig. 7). Percent of area with hot spots, defined as grid-volume integrated total dissipation exceeding 0.5 MW (corresponding to approximately 10^{-2} W m^{-2} depth-integrated dissipation) is 7 % for M_2, 11 % for K_1, and 15 % for the sum of M_2 and K_1. Total dissipation integrated over the domain is 314 and 617 MW for the M_2 and K_1 constituents, respectively. Dissipation of diurnal energy is concentrated on the northern flanks of the plateau, around the CEAREX-O drift site, over the shallow part of the plateau near the MIZEX83 drift, and

I. Fer et al.

around 17–18° E north of Svalbard. Dissipation of semidiurnal energy shows a similar pattern, but with relatively less pronounced dissipation near the CEAREX-O drift site. There is a patch of elevated dissipation near Station 4 where the highest mixing rates were recorded during our cruise (Fig. 4). These locations of energetic turbulence also coincide with regions of large barotropic tide velocities. The maximum tidal velocity amplitudes during one spring-neap cycle exceed $0.4\,\mathrm{m\,s^{-1}}$ in localized regions over the plateau and approach $1\,\mathrm{m\,s^{-1}}$ over the shelf north of Svalbard east of our Station 4. Over the plateau, the largest tidal velocity is near the seamount where D'Asaro and Morison (1992) inferred eddy diffusivities greater than $10^{-4}\,\mathrm{m^2\,s^{-1}}$ from XCP-shear. Close to the CEAREX-O camp, on the northern flanks, the maximum tidal velocity is more than $5\,\mathrm{cm\,s^{-1}}$ greater than that at our stations.

The spatial variability is further investigated using the integrated conversion and radiation rates over volumes bounded by increasing isobaths, following Kang and Fringer (2012). The results for the M_2 and K_1 constituents are shown in Fig. 8 using 250 m depth bins. Cumulative rates between chosen isobaths are tabulated in Table 5. The barotropic tide is converted to internal tide at all depths, for both constituents. The semidiurnal conversion shows an increase at isobaths deeper than 1500 m (over the sloping sides of the plateau) and with a peak around the 3000 m isobath (Fig. 8a). The radiation is nil below the 750 m isobath, positive between 750 and 2000 m, and negative for deeper water. All of the semidiurnal energy converted at depths shallower than 750 m, and also the amount generated in deeper water which propagates into shallower depth, are thus dissipated over the shelves. The slope between 750 and 2000 m depth is a generation site for propagating internal tide (positive radiation). The deeper part of the slope is a sink, and dissipates the energy that is locally generated as well as the fraction that is radiated from the upper slope.

Volume-integrated conversion of K_1 (618 MW) is approximately twice that of M_2. Similar to the M_2 pattern, there is radiation away from the upper part of the slope, whereas the deeper slope is a sink for the baroclinic K_1 energy flux. The major source and sink regions are relatively more constrained by the isobaths for K_1 (1000–1500 and 1750–

2250 m) compared to a broader distributed M_2 (750–2000 and 2250–4000 m). Most of the dissipation occurs deeper than 1500 m. The dissipation curve shows an approximate local conversion-dissipation balance over the shallows and also on the deeper part of the slope, but the dissipation exceeds twice the conversion rates between 1500 and 2000 m depth; all the K_1 energy radiation from the upper slope is dissipated here.

6 Discussion

Internal waves are generated over critical slopes where the ratio $\gamma = \beta/\alpha$ is unity. Here β is the topographic slope and $\alpha = (\omega^2 - f^2)^{1/2}(N^2 - \omega^2)^{-1/2}$ is the characteristic along which linear internal waves with frequency ω propagate (i.e., the horizontal slope of the internal wave ray). Although the critical condition ($\gamma = 1$) is optimal, internal wave generation at supercritical slopes ($\gamma > 1$) is also common. The critical condition also leads to enhanced shear and turbulence (Eriksen, 1985). As the turning latitude where $\omega = f$ is approached, however, the non-linear terms become increasingly important and the parameter γ becomes a crude indicator of the potential for internal wave generation (Vlasenko et al., 2003). Poleward of the turning latitude (e.g., the location of YP with respect to the M_2 frequency), the linear theory does not allow propagation of the internal wave with $\omega \leq f$. Negative background vorticities, however, can effectively reduce the inertial frequency and thereby potentially allow for linear sub-inertial internal waves. We evaluate γ for the M_2 frequency, using an effective inertial frequency of $0.95f$, and the buoyancy frequency from the survey mean full-depth CTD profiles. Anticyclonic loops and negative background vorticity on the order of $10^{-5}\,s^{-1}$ were previously inferred from floats over YP (Gascard et al., 1995). For the M_2 constituent, the northwestern flanks and the seamount region on the plateau are characterized by values of γ between 0.8 and 1.2 (Fig. 9), which favour the generation of semidiurnal internal tides and suggest elevated shear and mixing, consistent with earlier observations.

The amplitude of depth-integrated baroclinic semidiurnal energy flux is about $20\,W\,m^{-1}$ at Stations 1 and 5, respectively, and can be compared to the values from

STORMTIDE (Fig. 9). The sampling is limited, however, the depth-integrated flux vectors shown in Fig. 9 suggest radiation of semidiurnal energy away from the southern YP where γ is near unity. The large semidiurnal fluxes apparent on the flanks of the YP and along the slope north of Svalbard (Fig. 6a) are also co-located with near-critical slopes.

Among the stations, there is no clear correlation between the depth-integrated dissipation rate and the depth-integrated total energy (HKE+APE) or the depth-integrated baroclinic energy flux (Table 2). Especially Station 4 with the largest integrated dissipation rate has integrated energy less than Station 2. It is possible that the semidiurnal fits are contaminated by the near-inertial energy input in the upper layers. Furthermore, there may be other processes than internal waves leading to increased dissipation at Station 4. On the other hand, the baroclinic energy flux convergence can account for a fraction of the observed dissipation rate. The observed depth-integrated semidiurnal baroclinic fluxes at Stations 1, 2 and 4 and the mooring location are directed away from the plateau (northeastward on the northern stations and west/southwestward on the southern stations, Table 2, see also the vectors in Fig. 9). If all the decrease in the energy flux between Stations 2 and 4 were accounted for by turbulent dissipation over the 74 km separation, we obtain approximately $0.2\,\mathrm{mW\,m^{-2}}$ depth-integrated dissipation rate, comparable to the values in Table 4. Between Station 1 and the mooring location, from the flux divergence we obtain a depth-integrated dissipation of 0.03 and $0.26\,\mathrm{mW\,m^{-2}}$ by using XCP data and VM-ADCP data, respectively.

A crude estimate of the total energy dissipated over the YP can be made from observations as follows. We use the same domain surface area of $2 \times 10^{11}\,\mathrm{m^2}$ and the mean water depth of 2300 m inferred from the model. We choose two representative ε profiles; a lower bound ($\varepsilon_{2300\,\mathrm{m\text{-}min}}$) and an upper bound ($\varepsilon_{2300\,\mathrm{m\text{-}max}}$), each constructed to 2300 m depth. For the lower and upper bounds, we extend the $\varepsilon_{\min}$ and $\varepsilon_{\max}$ profile, respectively, of Stations 1 and 2 to 2300 m depth. Station 2, comparably to Station 3, is representative of the typical upper level of dissipation rates over the Yermak Plateau, excluding localized, enhanced dissipation observed on the northwestern flanks and

the seamount over the plateau. At such locations where the bottom topography is near critical to the semidiurnal waves (Fig. 9), the dissipation profile of Station 4 would be more appropriate. Using $\varepsilon_{2300\,m\text{-min}}$ and $\varepsilon_{2300\,m\text{-max}}$, the lower and upper bounds on the total energy dissipated are then 100 and 700 MW, respectively. Assuming 10 % of the region is characterized by exceptional enhanced dissipation rates (hot spots, Sect. 5), using 2300 m integrated dissipation from Station 4, 400 MW can be attributed to localized mixing regions. The bounds on the dissipation rate, including the hot spots, are thus 490 and 1030 MW. This estimate of the total dissipation includes a contribution from dissipation of internal tides (of diurnal and semidiurnal period) as well as other contributions such as turbulence due to mean shear.

The domain-integrated dissipation from STORMTIDE is 931 MW (sum of K_1 and M_2, where M_2 is 314 MW), in good agreement with the range inferred from the observations, and suggests that almost the entire dissipation (below 50 m depth) can be explained by the dissipation of baroclinic tidal energy. Using a global domain numerical model with 10 vertical layers, Simmons et al. (2004) report approximately 1 GW of M_2 conversion rate in the Fram Strait-Yermak Plateau region. Their box for the calculation of this domain covers 76° N to 90° N between 20° W and 15° E. For the same domain, we obtain 0.62 GW for M_2 and 0.63 GW of K_1 from STORMTIDE. According to our model result in the Fram Strait-Yermak Plateau region, about 50 % of the M_2 conversion, and almost 100 % of the K_1 conversion occurs over the YP. Our observed estimates of dissipation, in agreement with the model results, then suggest that 40 to 80 % of the energy contained in the internal tides in this extended region is dissipated around the YP.

The volume-integrated total dissipation can be converted to an eddy diffusivity using the Osborn model (Osborn, 1980), which can then be related to turbulent vertical heat flux using the mean vertical temperature gradient. We extracted annual average temperature and salinity profiles from the Polar Science Centre Hydrographic Climatology (Steele et al., 2001), from 125 grid points in the domain used in the YP energetics calculations. Domain-averaged annual mean temperature profile below 100 m increases with depth at a rate of 1°C per 100 m down to the core of the Atlantic layer at 250 m

Title Page

Abstract | Introduction

Conclusions | References

Tables | Figures

|◄ | ►|

◄ | ►

Back | Close

Full Screen / Esc

Printer-friendly Version

Interactive Discussion

depth below which the temperature decreases. If the entire dissipation takes place in this 150 m thick layer between 100 and 250 m (average $N^2 = 1.5 \times 10^{-5}\,\text{s}^{-2}$), the average upward turbulent heat flux is obtained as $17\,\text{W}\,\text{m}^{-2}$. This value is comparable to the average ocean-to-ice heat flux of $22\,\text{W}\,\text{m}^{-2}$ measured by McPhee et al. (2003) in the YP region. The dissipation of baroclinic tidal energy is thus a significant contributor to turbulent mixing and cooling of the Atlantic layer north of Svalbard.

7 Conclusions

Observations made in summer 2007 over the southern part of the Yermak Plateau (YP), together with results from a global high resolution ocean circulation and tide model simulation are used to investigate the role of tides, topography and internal waves in turbulent mixing near the YP. The plateau located northwest of Svalbard is of interest because it is the main topographic obstacle for the Atlantic water carried by the West Spitsbergen Current to the Arctic. Tidal forcing, barotropic to baroclinic energy conversion rates, baroclinic energy fluxes and dissipation rates in the region are discussed.

Depth-integrated conversion rates, baroclinic energy fluxes and dissipation rates show large spatial variability over the YP. The energetics are dominated by the K_1 and M_2 constituents. The volume-integrated conversion rate over the region enclosing the topographic feature is 322 MW for M_2 and 618 MW for K_1. This corresponds to about 50 % of the M_2 and approximately all of the K_1 conversion in a larger domain covering the entire Fram Strait, extended to the North Pole (76–90° N, 20° W–15° E). Despite the large energy conversion into internal tides, a negligible fraction propagates out of the YP region, implying substantial local dissipation. The suggested enhanced levels of dissipation are supported by past observations showing high dissipation rates and strong mixing over the upper slope on the northern flanks (Hunkins, 1986; Padman and Dillon, 1991) and in the vicinity of a seamount over the plateau (D'Asaro and Morison, 1992). When a plausible negative background relative vorticity is allowed, we find the

bottom topography in these regions critical to the semidiurnal frequency. Similar bottom slopes are also typical over the shelf north of Svalbard, close to one of our station with the largest mixing rates.

An approximate local conversion–dissipation balance is inferred over regions shallower than 1000 m, and also in the deep part of the sloping flanks, deeper than about 2000 m. On average, there is radiation of the baroclinic K_1 and M_2 energy away from the upper part of the slope, which is dissipated over the deeper isobaths. Most of the dissipation occurs in water deeper than 1500 m. Approximately the entire K_1 energy radiated in the region is dissipated between 1000 and 1500 m depth. The dissipation of the radiated M_2 energy is broadly distributed over the 2250 to 4000 m isobaths.

From observations, we infer upper and lower bounds on the total dissipation rate of 490 and 1030 MW, of which approximately 400 MW can be attributed to the contribution of hot spots. The domain-integrated dissipation from STORMTIDE is in good agreement with the range inferred from the observations, and suggests that almost all the dissipation in the region can be attributed to the dissipation of baroclinic tidal energy. Using the climatological temperature profiles and stratification averaged above the core of the Atlantic layer, the volume-integrated total dissipation leads to an average upward turbulent heat flux of $17\,\mathrm{W\,m^{-2}}$, comparable to the average ocean-to-ice heat flux measured in the YP region. The dissipation of baroclinic tidal energy is thus a significant contributor to turbulent mixing and cooling of the Atlantic layer north of Svalbard. The role of tidal forcing in the heat budget of the Arctic Ocean in general merits further studies.

References

Althaus, A. M., Kunze, E., and Sanford, T. B.: Internal tide radiation from Mendocino Escarpment, J. Phys. Oceanogr., 33, 1510–1527, 2003. 2259

Amante, C. and Eakins, B.: ETOPO1 1 Arc-Minute Global Relief Model: Procedures, Data Sources and Analysis, NOAA Technical Memorandum NESDIS NGDC-24, National Geophysical Data Center, NOAA, doi:10.7289/V5C8276M, 2009. 2279

Arneborg, L. and Liljebladh, B.: Overturning and dissipation caused by baroclinic tidal flow near the sill of a fjord basin, J. Phys. Oceanogr., 39, 2156–2174, 2009. 2260

Baines, P. G.: On internal tide generation models, Deep-Sea Res. Pt. I, 29, 307–338, 1982. 2253

Chen, C., Gao, G., Qi, J., Proshutinsky, A., Beardsley, R. C., and Kowalik, Z., Lin, H., and Cowles, G.: A new high-resolution unstructured-grid finite-volume Arctic Ocean model (AO-FVCOM): an application for tidal studies, J. Geophys. Res., 114, C08017, doi:10.1029/2008JC004941, 2009. 2261

Cummins, P. F., Cherniawsky, J. Y., and Foremann, M. G. G.: North Pacific internal tides from the Aleutian Ridge: altimeter observations and modeling, J. Mar. Res., 59, 167–191, 2001. 2261

D'Asaro, E. A. and Morison, J. H.: Internal waves and mixing in the Arctic Ocean, Deep-Sea Res., 39, S459–S484, 1992. 2247, 2248, 2264, 2268, 2283, 2284, 2285

Egbert, G. D. and Ray, R. D.: Significant dissipation of tidal energy in the deep ocean inferred from satellite altimeter data, Nature, 405, 775–778, 2000. 2251

Eriksen, C. C.: Implications of ocean bottom reflection for internal wave spectra and mixing, J. Phys. Oceanogr., 15, 1145–1156, 1985. 2265

Fer, I.: Scaling turbulent dissipation in an Arctic fjord, Deep-Sea Res. Pt. II, 53, 77–95, 2006. 2250

Fer, I. and Sundfjord, A.: Observations of upper ocean boundary layer dynamics in the marginal ice zone, J. Geophys. Res., 112, C04012, doi:10.1029/2005JC003428, 2007. 2248

Fer, I., Skogseth, R., and Geyer, F.: Internal waves and mixing in the Marginal Ice Zone near the Yermak Plateau, J. Phys. Oceanogr., 40, 1613–1630, 2010. 2247, 2248

Foreman, M. G. G., Cherniawsky, J. Y., and Ballantyne, V. A.: Versatile harmonic tidal analysis: improvements and applications, J. Atmos. Ocean. Tech., 26, 806–817, doi:10.1175/2008jtecho615.1, 2009. 2251

Tidal mixing near the Yermak Plateau

I. Fer et al.

Title Page

Abstract	Introduction
Conclusions	References
Tables	Figures

◄◄   ►►

◄   ►

Back   Close

Full Screen / Esc

Printer-friendly Version

Interactive Discussion

Garrett, C. and Kunze, E.: Internal tide generation in the deep ocean, Annu. Rev. Fluid. Mech., 39, 57–87, 2007. 2247

Gascard, J. C., Richez, C., and Roaualt, C.: New insights on large-scale oceanography in Fram Strait: the West Spitsbergen Current, in: Arctic Oceanography, Marginal Ice Zones and Continental Shelves, edited by: Smith Jr., W. O. and Grebmeier, J., Vol. 49, chap. 5, 131–182, AGU, Washington DC, 1995. 2265

Gerkema, T. and van Haren, H.: Internal tides and energy fluxes over Great Meteor Seamount, Ocean Sci., 3, 441–449, doi:10.5194/os-3-441-2007, 2007. 2256, 2257, 2261

Hunkins, K.: Anomalous diurnal tidal currents on the Yermak Plateau, J. Mar. Res., 44, 51–69, 1986. 2247, 2268

Jeon, C., Park, J.-H., Varlamov, S. M., Yoon, J.-H., Kim, Y. H., Seo, S., Park, Y.-G., Min, H. S., Lee, J. H., and Kim, C.-H.: Seasonal variation of semidiurnal internal tides in the East/Japan Sea, J. Geophys. Res., 119, 2843–2859, doi:10.1002/2014JC009864, 2014. 2261

Jungclaus, J. H., Keenlyside, N., Botzet, M., Haak, H., Luo, J. J., Latif, M., Marotzke, J., Mikolajewicz, U., and Roeckner, E.: Ocean Circulation and Tropical Variability in the Coupled Model ECHAM5/MPI-OM, J. Climate, 19, 3952–3972, doi:10.1175/JCLI3827.1, 2006. 2250

Kang, D. J. and Fringer, O.: Energetics of barotropic and baroclinic tides in the Monterey Bay area, J. Phys. Oceanogr., 42, 272–290, 2012. 2248, 2252, 2261, 2262, 2264

Klymak, J. M., Pinkel, R., and Rainville, L.: Direct breaking of the internal tide near topography: Kaena ridge, Hawaii, J. Phys. Oceanogr., 38, 380–399, 2008. 2247

Klymak, J. M., Alford, M. H., Pinkel, R., Lien, R. C., Yang, Y. J., and Tang, T. Y.: The breaking and scattering of the internal tide on a continental slope, J. Phys. Oceanogr., 41, 926–945, doi:10.1175/2010jpo4500.1, 2011. 2261

Kowalik, Z. and Proshutinsky, A. Y.: The Arctic Ocean tides, in: The Polar Oceans and their role in shaping the global environment, edited by: Johannessen, O., Muench, R., and Overland, J., AGU, 137–158, 1993. 2249

Kunze, E., Rosenfeld, L. K., Carter, G. S., and Gregg, M. C.: Internal waves in Monterey Submarine Canyon, J. Phys. Oceanogr., 32, 1890–1913, 2002. 2252, 2253, 2262

Leaman, K. D. and Sanford, T. B.: Vertical energy propagation of inertial waves: a vector spectral analysis of velocity profiles, J. Geophys. Res., 80, 1975–1978, 1975. 2255

McPhee, M. G., Kikuchi, T., Morison, J. H., and Stanton, T. P.: Ocean-to-ice heat flux at the North Pole environmental observatory, Geophys. Res. Lett., 30, 2274, doi:10.1029/2003GL018580, 2003. 2248, 2268

Title Page

Abstract | Introduction

Conclusions | References

Tables | Figures

|◄ | ►|

◄ | ►

Back | Close

Full Screen / Esc

Printer-friendly Version

Interactive Discussion

Merrifield, M. A. and Holloway, P. E.: Model estimates of M_2 internal tide energetics at the Hawaiian Ridge, J. Geophys. Res., 107, 3179, doi:10.1029/2001jc000996, 2002. 2248

Müller, M.: On the space- and time-dependence of barotropic-to-baroclinic tidal energy conversion, Ocean Model., 72, 242–252, doi:10.1016/j.ocemod.2013.09.007, 2013. 2248

5 Müller, M., Cherniawsky, J. Y., Foreman, M. G. G., and von Storch, J. S.: Global M_2 internal tide and its seasonal variability from high resolution ocean circulation and tide modeling, Geophys. Res. Lett., 39, L19607, doi:10.1029/2012gl053320, 2012. 2249, 2250, 2251

Müller, M., Cherniawsky, J., Foreman, M. G., and von Storch, J.-S.: Seasonal variation of the M_2 tide, Ocean Dyn., 64, 159–177, doi:10.1007/s10236-013-0679-0, 2014. 2251

10 Nash, J. D., Alford, M. H., and Kunze, E.: Estimating internal wave energy fluxes in the ocean, J. Atmos. Ocean. Tech., 22, 1551–1570, 2005. 2252, 2253

Nash, J. D., Kunze, E., Lee, C. M., and Sanford, T. B.: Structure of the baroclinic tide generated at Kaena Ridge, Hawaii, J. Phys. Oceanogr., 36, 1123–1135, 2006. 2257, 2259

Nycander, J.: Generation of internal waves in the deep ocean by tides, J. Geophys. Res., 110,
15 C10028, doi:10.1029/2004jc002487, 2005. 2251

Osborn, T. R.: Estimates of the local rate of vertical diffusion from dissipation measurements, J. Phys. Oceanogr., 10, 83–89, 1980. 2267

Padman, L. and Dillon, T.: Turbulent mixing near the Yermak Plateau during the coordinated Eastern Arctic Experiment, J. Geophys. Res., 96, 4769–4782, 1991. 2247, 2248, 2262,
20 2268, 2283, 2284, 2285

Padman, L., Plueddemann, A. J., Muench, R. D., and Pinkel, R.: Diurnal tides near the Yermak Plateau, J. Geophys. Res., 97, 12639–12652, 1992. 2247, 2248, 2261

Phillips, O. M.: The Dynamics of the Upper Ocean, Cambridge Univ. Press, Cambridge, UK, 2nd Edn., 1977. 2255

25 Plueddemann, A. J.: Internal wave observations from the Arctic Environmental Drifting Buoy, J. Geophys. Res., 97, 12619–12638, 1992. 2247, 2248

Rudnick, D. L., Boyd, T. J., Brainard, R. E., Carter, G. S., Egbert, G. D., Gregg, M. C., Holloway, P. E., Klymak, J. M., Kunze, E., Lee, C. M., Levine, M. D., Luther, D. S., Martin, J. P., Merrifield, M. A., Moum, J. N., Nash, J. D., Pinkel, R., Rainville, L., and Sanford, T. B.: From
30 tides to mixing along the Hawaiian Ridge, Science, 301, 355–357, 2003. 2261

Simmons, H., Chang, M.-H., Chang, Y.-T., Chao, S.-Y., Fringer, O., Jackson, C., and Ko., D.: Modeling and prediction of internal waves in the South China Sea, Oceanography, 24, 88–99, doi:10.5670/oceanog.2011.97, 2011. 2257

Title Page

Abstract   Introduction

Conclusions   References

Tables   Figures

|◄   ►|

◄   ►

Back   Close

Full Screen / Esc

Printer-friendly Version

Interactive Discussion

Simmons, H. L., Hallberg, R. W., and Arbic, B. K.: Internal wave generation in a global baroclinic tide model, Deep-Sea Res. Pt. II, 51, 3043–3068, 2004. 2248, 2251, 2267

Sirevaag, A. and Fer, I.: Early spring oceanic heat fluxes and mixing observed from drift stations north of Svalbard, J. Phys. Oceanogr., 39, 3049–3069, 2009. 2248

Stammer, D., Ray, R. D., Andersen, O. B., Arbic, B. K., Bosch, W., Carrère, L., Cheng, Y., Chinn, D. S., Dushaw, B. D., Egbert, G. D., Erofeeva, S. Y., Fok, H. S., Green, J. A. M., Griffiths, S., King, M. A., Lapin, V., Lemoine, F. G., Luthcke, S. B., Lyard, F., Morison, J., Müller, M., Padman, L., Richman, J. G., Shriver, J. F., Shum, C. K., Taguchi, E., and Yi, Y.: Accuracy assessment of global barotropic ocean tide models, Rev. Geophys., online first, doi:10.1002/2014RG000450, 2014. 2251

Steele, M., Morley, R., and Ermold, W.: PHC: A global ocean hydrography with a high-quality Arctic Ocean, J. Climate, 14, 2079–2087, 2001. 2267

Tanaka, Y., Yasuda, I., Hasumi, H., Tatebe, H., and Osafune, S.: Effects of the 18.6 yr modulation of tidal mixing on the North Pacific bidecadal climate variability in a coupled climate model, J. Climate, 25, 7625–7642, doi:10.1175/Jcli-D-12-00051.1, 2012. 2248

Terker, S. R., Girton, J. B., Kunze, E., Klymak, J. M., and Pinkel, R.: Observations of the internal tide on the California continental margin near Monterey Bay, Cont. Shelf Res., 82, 60–71, doi:10.1016/j.csr.2014.01.017, 2014. 2262

Vlasenko, V., Stashchuk, N., Hutter, K., and Sabinin, K.: Nonlinear internal waves forced by tides near the critical latitude, Deep-Sea Res. Pt. I, 50, 317–338, 2003. 2265

Wijesekera, H., Padman, L., Dillon, T., Levine, M., Paulson, C., and Pinkel, R.: The application of internal-wave dissipation models to a region of strong mixing, J. Phys. Oceanogr., 23, 269–286, 1993. 2247

Title Page

Abstract | Introduction

Conclusions | References

Tables | Figures

|◄ | ►|

◄ | ►

Back | Close

Full Screen / Esc

Printer-friendly Version

Interactive Discussion

Discussion Paper | Discussion Paper | Discussion Paper | Discussion Paper |

OSD

11, 2245–2287, 2014

Tidal mixing near the Yermak Plateau

I. Fer et al.

Title Page

Abstract | Introduction

Conclusions | References

Tables | Figures

|◄ | ►|

◄ | ►

Back | Close

Full Screen / Esc

Printer-friendly Version

Interactive Discussion

Table 1. Summary of station position, sampling duration, and vertical coverage. 5-M is the mooring located near Station 5. Water depth is the mean ± one SD over the station duration. The corresponding stretched depth (in stretched meter, sm) and the covered fraction are listed for a range of 3–500 m for MSS and 12–360 m for the VM-ADCP.

Station	Latitude (N)	Longitude (E)	Duration (h) MSS/ADCP	Water Depth (m)	Stretched Depth (sm)	Coverage (%)
1	80˚7.95′	4˚18.10′	24.1/24.3	1253 ± 57	1147	64/52
2	80˚25.14′	6˚55.24′	23.1/24.7	637 ± 9	715	84/67
3	80˚34.0′	9˚46.73′	22.7/8.8	1000 ± 86	828	66/50
4	80˚0.57′	9˚59.25′	24.4/18.8	484 ± 4	567	99/73
5	80˚0.1′	5˚58.10′	24.2/4.6	879 ± 29	988	70/49
5-M	79˚59.78′	5˚55.95′	195.5/15.1[a]	889	990	75[b]

[a] Duration of Microcat sampling/Duration of Longranger sampling.
[b] Percentage of the stretched depth covered by the moored Microcats.

Table 2. Semidiurnal energetics at observations stations. Results are shown for mode 1 and sum of the first 3 modes. An overbar indicates integration over depth. 1-XCP is Station 1 with results inferred from the XCP profiles. 5-M is the mooring located near Station 5.

Station	$10^3 \times$ HKE (J m^{-3})	$10^3 \times$ APE (J m^{-3})	R	$\overline{\text{HKE}}$ (J m^{-2})	$\overline{\text{AKE}}$ (J m^{-2})	F_u (W m^{-1})	F_v (W m^{-1})
1-XCP	93/326	3/20	32/16	112/416	23/236	−9/−22	−13/−3
1	32/85	1/24	24/4	39/88	11/240	−6/−12	4/7
2	83/87	7/10	11/9	82/84	15/22	24/24	2/2
3	–	4/90	–	–	5/185	–	–
4	40/70	1/25	26/3	25/43	1/19	9/9	2/4
5	–	8/49	–	–	40/358	–	–
5-M	132/378	2/3	66/120	70/179	11/18	−4/−22	3/7

Table 3. Depth-integrated dissipation rate. Integrations down to 500 m follow the station mean ε profiles. Integrations from 50 m to the bottom use the assumed minimum and maximum ε profiles described in the text.

Station	$\int_0^{500\,m} \rho\varepsilon\mathrm{d}z$ mW m^{-2}	$\int_{50\,m}^{500\,m} \rho\varepsilon\mathrm{d}z$ mW m^{-2}	$\int_{50\,m}^{H} \rho\varepsilon_{min}\mathrm{d}z$ mW m^{-2}	$\int_{50\,m}^{H} \rho\varepsilon_{max}\mathrm{d}z$ mW m^{-2}
1	3.7	0.4	0.3	0.8
2	2.3	0.6	0.7	0.8
3	0.8	0.5	0.6	1.0
4	1.9	1.3	1.3	1.3
5	0.9	0.3	0.2	0.5

Table 4. Depth-integrated baroclinic fluxes inferred from STORMTIDE using grid points within 10 km of the observation stations. **F** is listed as the average ± one standard deviation over the total number of grid points for the horizontal components (F_u, F_v), in units of $\mathrm{W\,m^{-1}}$ for the 4 major constituents.

Station	M_2	S_2	K_1	O_1
1	$(-19 \pm 22, -4 \pm 25)$	$(-5 \pm 5, -9 \pm 1)$	$(-17 \pm 51, 21 \pm 20)$	$(6 \pm 10, 1 \pm 4)$
2	$(1 \pm 2, -7 \pm 2)$	$(1 \pm 0, 0 \pm 0)$	$(3 \pm 4, 4 \pm 4)$	$(-1 \pm 1, 1 \pm 1)$
3	$(1 \pm 7, -2 \pm 17)$	$(1 \pm 1, -1 \pm 1)$	$(7 \pm 6, 2 \pm 3)$	$(2 \pm 2, 2 \pm 2)$
4	$(2 \pm 5, 3 \pm 11)$	$(0 \pm 0, 0 \pm 1)$	$(10 \pm 6, -2 \pm 6)$	$(1 \pm 1, -1 \pm 0)$
5	$(-23 \pm 74, 7 \pm 69)$	$(7 \pm 16, -9 \pm 10)$	$(33 \pm 3, 13 \pm 9)$	$(5 \pm 2, 2 \pm 3)$

Table 5. Volume-integrated conversion and radiation rates for the M_2 and K_1 constituents, bounded by selected isobaths. Shallower than 250 m (not listed), there is approximately 10 MW conversion, for both M_2 and K_1, balanced by local dissipation.

Isobath (m)	M_2 Conversion (MW)	M_2 Radiation (MW)	M_2 Dissipation (MW)	K_1 Conversion (MW)	K_1 Radiation (MW)	K_1 Dissipation (MW)
250–750	19	0	19	42	−4	46
750–2000	85	80	5	175	−23	198
2000–5000	218	−72	290	401	28	373

Full Screen / Esc

Printer-friendly Version

Interactive Discussion
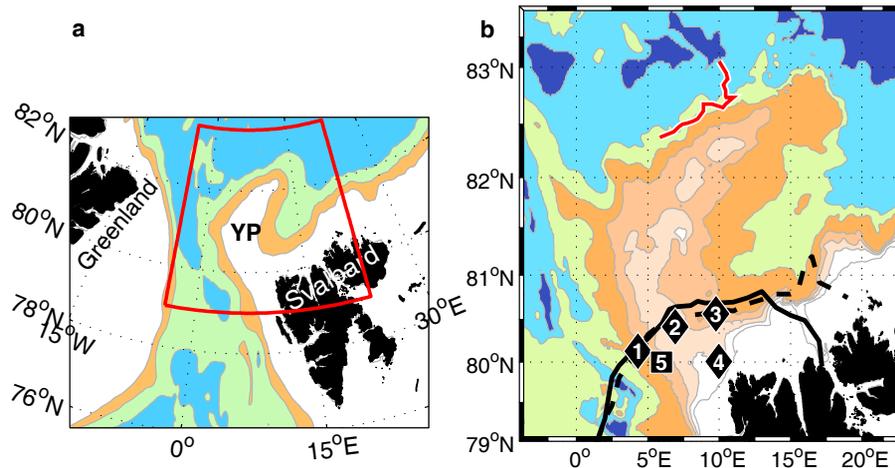
Figure 1. (a) Location map of the study area with the Yermak Plateau (YP) enlarged in **(b)**. Iso-baths are drawn at 1000 m intervals (ETOPO5) in **(a)**, and at 250 m intervals to 1000 m followed by 1000 m intervals (ETOPO1, Amante and Eakins, 2009) in **(b)**. Stations 1 to 5 are marked. Station 5 is co-located with the short-term mooring (rectangle). The drift of the CEAREX-O camp is shown by the white-enveloped red line on the northern flanks. The ice-edge digitized from high-resolution ice charts (http://polarview.org/services/hric.htm) provided by the Norwegian Meteorological Institute are shown for 23 (dashed) and 25 July 2007 (solid).
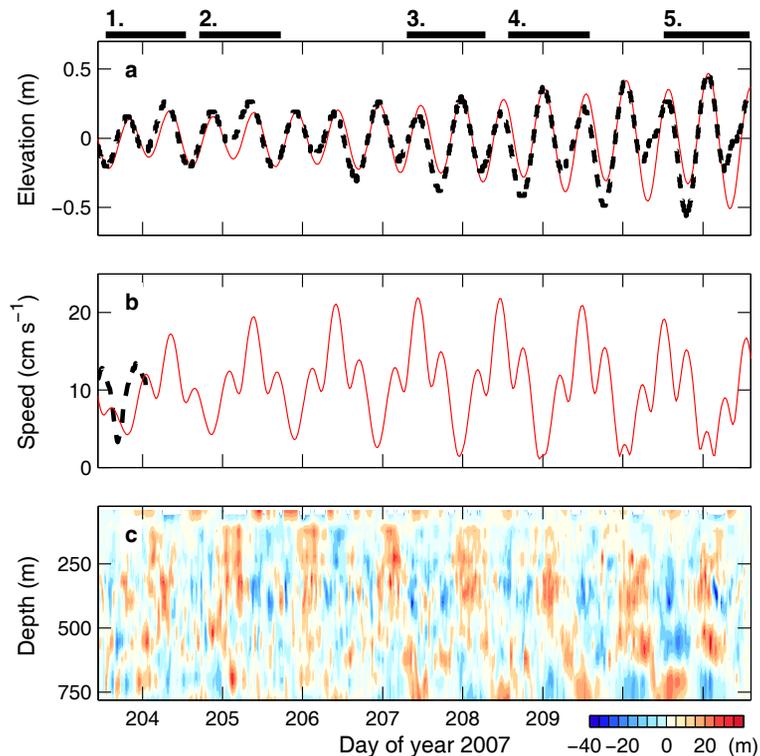
Figure 2. Time series at Station 5 (see also Fig. 1) of **(a)** tidal surface elevation from STORMTIDE (red, sum of 8 major constituents) and near-bottom pressure anomaly from the deepest moored instrument (dashed), **(b)** tidal current from STORMTIDE (red, sum of M_2, K_1, S_2 and O_1) and depth-averaged current measured by the moored instruments (dashed), and **(c)** vertical isopycnal displacements. Bars on top show the duration of stations 1 to 5.
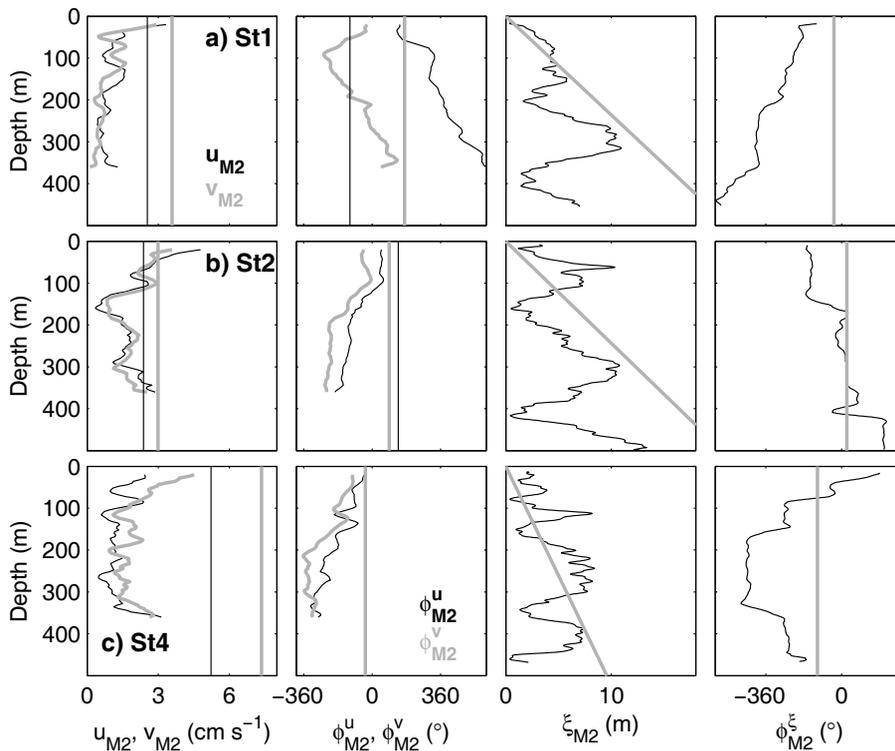
Figure 3. Profiles of amplitude and phase of u, v, and ξ obtained from the semidiurnal fits to VM-ADCP and MSS profiles at Stations **(a)** 1, **(b)** 2 and **(c)** 4. Also shown are the corresponding barotropic amplitude (vertical lines for u and v, and slanted lines for ξ) and phase (vertical lines), inferred from identical harmonic analysis of the depth-averaged currents and profile of barotropic displacement.
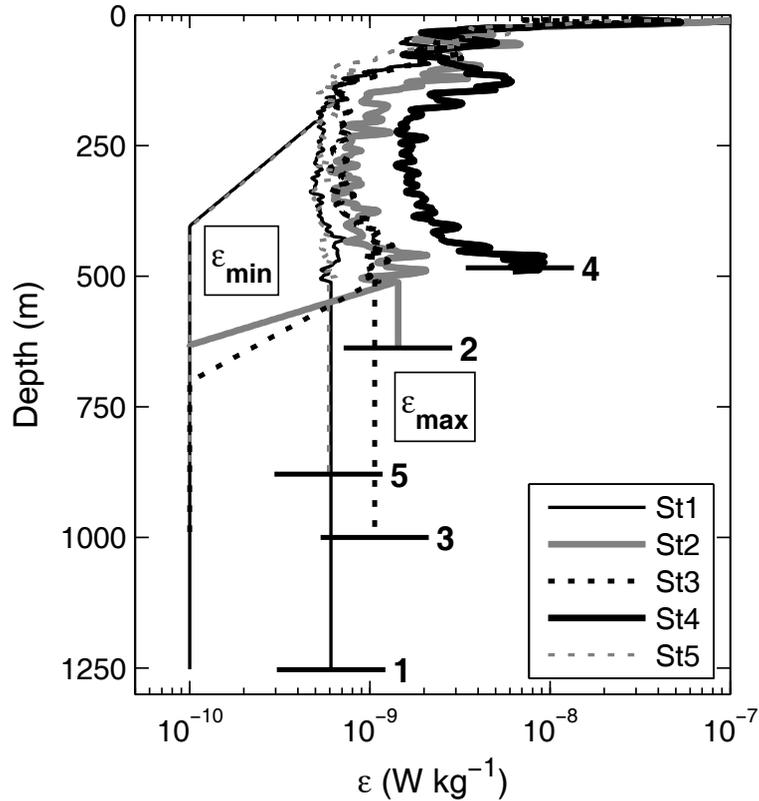
Figure 4. Dissipation rate profiles for Stations 1 to 5. Horizontal lines with the station number indicated mark the mean echo sounder depth for the station. Observed, station-mean profiles are shown in the upper 500 m. Full depth profiles used in calculating depth-integrated ε are also shown for the lower bound ε_{min} and the upper bound ε_{max}.

Title Page

Abstract | Introduction

Conclusions | References

Tables | Figures

|◀ | ▶|

◀ | ▶

Back | Close

Full Screen / Esc

Printer-friendly Version

Interactive Discussion

Figure 5. Barotropic tidal flux obtained from STORMTIDE for **(a)** M_2 and **(b)** K_1 constituents. Isobaths (grey) are drawn at 500 m intervals from the model topography. The colour is the amplitude of the corresponding flux with colorbar on the right. Every fourth vector is shown with scale indicated. Station positions (open circles), and the drift of CEAREX-O (Padman and Dillon, 1991) (red line over the northern flank) and MIZEX83 (D'Asaro and Morison, 1992) (red line over the plateau) are shown for reference.
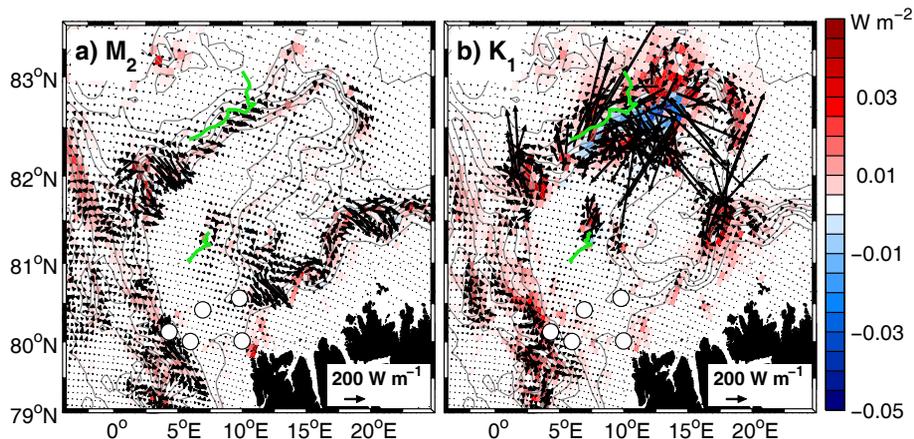
Figure 6. Barotropic to baroclinic conversion rate (color) and the depth-integrated baroclinic energy fluxes (arrows) obtained from STORMTIDE for **(a)** M_2 and **(b)** K_1 constituents. Isobaths (gray) are drawn at 500 m intervals from the model topography. Station positions (open circles) and the drift of CEAREX-O (Padman and Dillon, 1991) and MIZEX83 (D'Asaro and Morison, 1992) (green) are shown for reference.
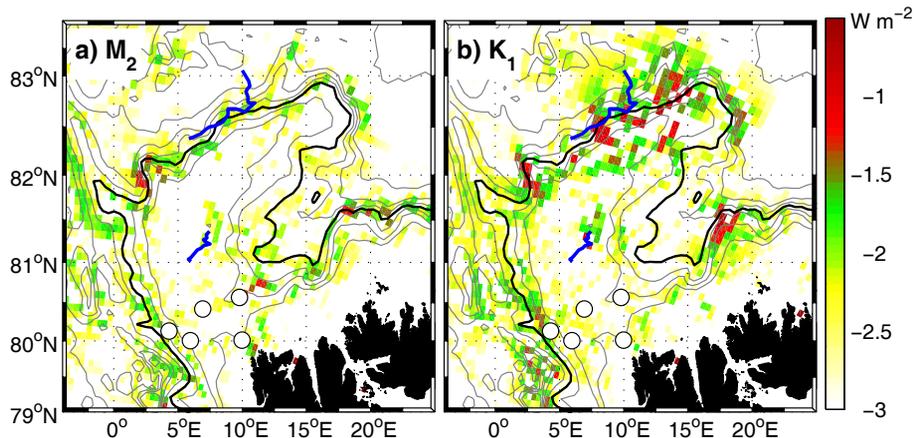
Figure 7. Depth-integrated dissipation rate, presented in base-10 logarithm, for **(a)** M_2 and **(b)** K_1 constituents obtained from STORMTIDE. Isobaths (gray) drawn at 500 m intervals is from the model topography. The 2000 m isobath is drawn in black for reference. Station positions (open circles), and the drift of CEAREX-O (Padman and Dillon, 1991) and MIZEX83 (D'Asaro and Morison, 1992) are also shown.
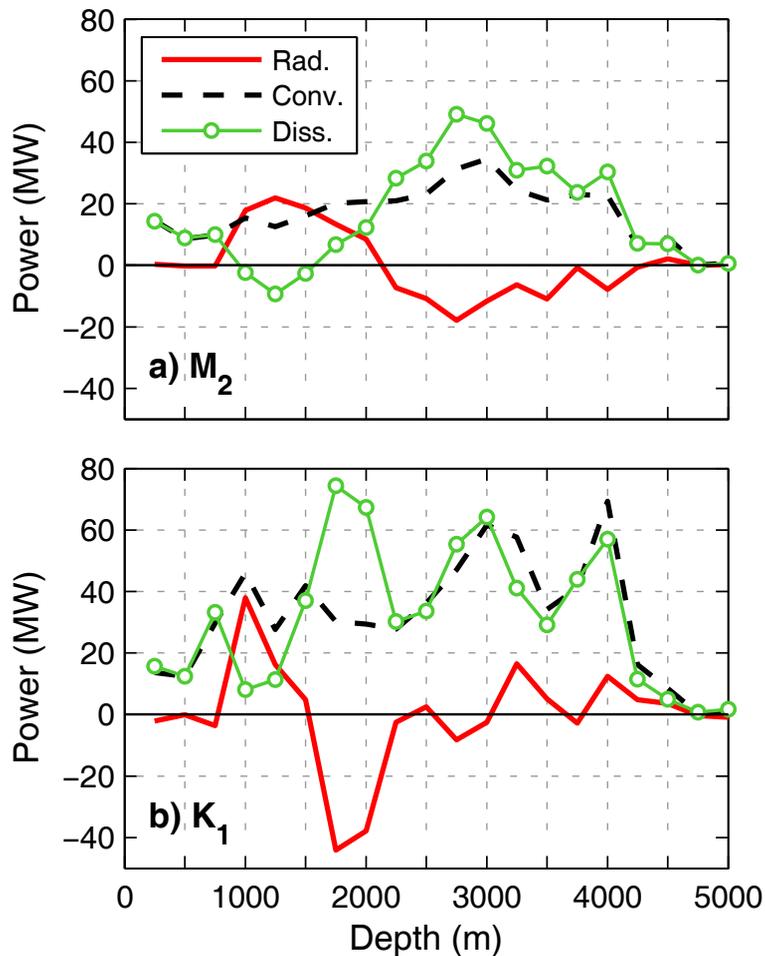
Figure 8. Total baroclinic radiation (red), conversion (dashed black), and dissipation (green, circles) for the **(a)** M_2 and **(b)** K_1 constituents, integrated in 250 m isobath bounded volumes.
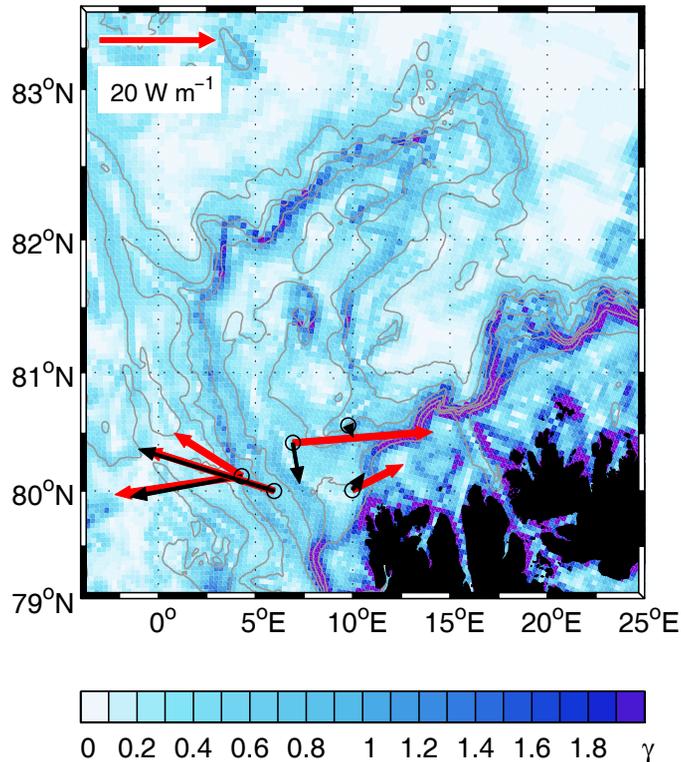
Figure 9. Contours of γ, the ratio of semidiurnal internal wave characteristic to the bottom slope. An effective inertial frequency of $0.95f$ (i.e., assuming negative, anti-cyclonic, relative vorticity of $0.05f$) is used in the calculations. Superimposed are the isobaths (250, 500, 750, 1000, 1500, 2000 and 3000 m), station positions (circles) and the depth-integrated baroclinic semidiurnal flux (arrows) with scale given on the top left. Red arrows are inferred from the observations whereas the black arrows are inferred from STORMTIDE averaged over 10 km range of the stations. At Station 1 the two observed flux vectors are obtained from the VM-ADCP (directed northwest) and the XCP data.